Optimal Pole Ratio of Spoke-type Permanent Magnet Vernier Machines for Direct-drive Applications

Yu Zhao, Dawei Li, *Senior Member*, *IEEE*, Xiang Ren, Ronghai Qu, *Fellow*, *IEEE,* Jianbo Sun, and Ping Yu

***Abstract*—Due to magnetic gearing effects, spoke-type permanent magnet vernier machines (ST-PMVMs) have the merit of high torque density, where an extra torque amplification coefficient, i.e., pole ratio (the pole-pair ratio of PMs to armature windings) is introduced. However, different from surface-mounted PMVM, the variation of torque against pole ratio in ST-PMVMs is non-linear, which is increased at first and then decreased. This article is devoted to identify the optimal pole ratio of ST-PMVMs by equivalent magnetic circuit model. It is found that except the P_r^{th} air-gap magnetomotive force (MMF) harmonic having the same pole-pair of PM, the P_a^{th} air-gap MMF harmonic having the same pole-pair of armature winding is also induced due to the modulation of doubly salient air-gap structure. The P_r^{th} MMF harmonic produces positive torque, while P_a^{th} MMF harmonic produces negative torque. With the increase of pole ratio, the proportion of P_a^{th} MMF harmonic as well as negative torque is increased, which reduces the advantages of high pole ratio coefficient. Further, the influence of dimension parameters on the performance of ST-PMVMs under different pole ratio are investigated. Results show that ST-PMVMs with pole ratio 2.6 have high torque density, low cogging torque and high power factor simultaneously. Finally, a prototype is manufactured to validate the analysis.**

***Index Terms*—Spoke-type permanent magnet machines (ST-PMVMs), Pole ratio, Back electromagnetic force (EMF) and torque capability.**

I. INTRODUCTION

COMBINED with the advantages of compact structure, high efficiency and free maintenance, direct-drive systems have attracted increasingly more attention. Driving motors as one of the key components, play critical role in the low-speed high-torque direct-drive applications, such as wind power generation, marine propulsion and electric vehicles (EVs).

Manuscript received October 8, 2021; revised December 15, 2021; accepted April 26, 2022. date of publication December 25, 2022; date of current version December 18, 2022.

This work was supported in part by the National Nature Science Foundation of China (NSFC) under Project 51977094 and in part by the National Key Research and Development Program of China under Grant 2017YFB0102400. (*Corresponding author: Dawei Li*.)

Y. Zhao, D. Li, X. Ren, R. Qu and J. Sun are with the State Key Laboratory of Advanced Electromagnetic Engineering and Technology, School of Electric al and Electronic Engineering, Huazhong University of Science and Technolog y, Wuhan, 430074, China (e-mail: yuzhao@hust.edu.cn; daweili@hust.edu.cn; renxiang_1993@hust.edu.cn; ronghaiqu@hust.edu.cn; jianbo.sun@hust.edu.c n).

P. Yu is the Jing-Jin Electric Technology (Zhengding) Co., Ltd (e-mail:ping. yu@jjecn.com).

Digital Object Identifier 10.30941/CESTEMS.2022.00057

Nowadays, it is the hot topic to research the driving motors satisfying high torque density, high power density and low torque ripples simultaneously [1]-[3]. And the research contents include: topology selection, control strategy, vibration and noise suppression, and so on.

At present, diverse machine topologies have been applied in direct-drive systems. As one of the PM-free machines, switch reluctance machines (SRMs) have been used in in-wheel applications owing to their simple structure and high reliability [4]. Whereas, they suffer from big noise and vibration. Moreover, induction machines (IMs) are also widely used, while they are very sensitive to saturation [5]. With the development of PM materials, PM machines have the merits of high torque density and high efficiency, which can be the better candidate for direct-drive application. And in [6], the performance of surface-mounted PM machines (SPMs) and interior PM machines (IPMs) for EVs are compared, where the two machines can achieve the similar rated power but that SPMs have barely no overload capability and face with the danger of irreversible demagnetization. In recent years, many novel PM machines, including PM vernier machines (PMVMs), flux switching machines and flux reversal machines, have drawn more and more attention owing to higher torque density [7]-[9]. Previous researches have indicated that the high torque density of which is attributed to the introduction of an extra torque amplification factor, that is, pole ratio (the pole-pair ratio of PM to armature winding), which reflects the magnetic field modulation effects.

Generally, neglecting saturation effects, the torque capability of PMVMs can be directly predicted by pole ratio. That is, the higher pole ratio, the higher torque capability. However, it is interesting that with the increase of pole ratio, the torque of ST-PMVMs is increased firstly and then decreased. In previous literatures [10], it is explained as the "flux barrier effects", where the flux paths are interrupted by permanent magnets having opposite magnetizing directions. Moreover, in [11], by analogy, it is pointed out that the rotor potential oscillation phenomenon is associated with ST-PMVMs, which is the critical problem removing the advantages of magnetic modulation effects. However, the study described above only qualitatively explains the torque decrease in high pole ratio ST-PMVMs. The nature of low torque capability of high pole ratio ST-PMVMs and the optimal pole ratio has seldom been investigated.

Moreover, the winding feature of PMVMs with different

pole ratio are not identical. According to slot/pole combination principle, the stator slot number of PMVMs is generally the pole-pair sum of armature winding and PM [12]. That is, under the fixed stator slot number, once the pole ratio is determined, the slot/pole combination and winding structure are also determined. Generally, the full-pitch distribution winding (coil pitch ≥ 3) have been widely used in PMVMs, where the pole ratio is higher than 5 [13]. The magnetic field modulation effects in which are remarkable, while the machines suffer from long end-windings and large copper losses. Recently, in [14-15], it is found that regular fractional slot concentrated winding permanent magnet synchronous machines (PMSMs) with coil pitch of 1 also exist the magnetic field modulation effects, which can be treated as the special flux modulation machines with pole ratio range of 1~2. Nevertheless, with the small pole ratio, it fail to take the advantage of modulation effects. Moreover, relevant scholars proposed fractional slot distribution winding PMVMs (coil pitch =2), which further extend the pole ratio range of 2~5. And compact end-winding and high torque density can be acquired at the same time [16].

Therefore, with a purpose of determining the optimal pole ratio of ST-PMVMs for direct-drive applications, the machine performance including air-gap MMF, air-gap flux density, back electromagnetic force (EMF) and electromagnetic torque under a wide pole ratio range are comprehensively analyzed and compared based on equivalent magnetic circuit model. Meanwhile, critical dimension parameters are also studied to provide the guidance for engineering designers.

The main contents are organized as follows: First, the air-gap MMF, air-gap flux density, EMF and torque of ST-PMVMs with different pole ratio are investigated considering the influence of opening slot stator in Section II, where the corresponding torque expression has been given, and the influence of pole ratio on torque is revealed. Second, Section III analyzes the critical dimension parameters that associated with pole ratio. Then, machine performance, in terms of no-load and on-load are comprehensively analyzed and compared, and the optimal pole ratio is determined, in section IV. The experimental results are discussed in Section V. Finally, Section VI presents the conclusion.

II. Analysis of Working Principles

A. Machine Model

The models of ST-PMVMs with different pole ratio *PR* are shown in Fig. 1, which are constructed with spoke-type PM rotors and the magnetizing direction of two adjacent PMs are opposite. As the counterpart, regular PMSM is also depicted in Fig. 1(d). And the only difference between ST-PMVMs and PMSM is stator slot shape, where half-closed slot has been used in PMSM. Based on slot/pole combination principle of ST-PMVMs [13], for any *m* phase symmetry winding, the stator slot number Z_s, PM rotor pole-pair P_r and armature winding pole-pair P_a should satisfy:

$$\begin{cases} Z_s = P_a + P_r \\ \dfrac{Z_s}{GCD(Z_s, P_a)} = mk, k = 1, 2, 3... \end{cases} \tag{1}$$

Further, stator slot number Z_s can be expressed as $6P_aq$, where q is the slot number per pole and phase. Then, the pole ratio *PR* can be given as:

$$PR = \frac{P_r}{P_a} = \frac{Z_s - P_a}{P_a} = 6q - 1 \tag{2}$$

Thus, at fixed stator slot number, once pole ratio is determined, the corresponding slot/pole combination and winding connection is determined. Take 18-stator-slot as examples, the feasible slot/pole combinations are listed in Table I. For the machine with pole ratio is larger than 5, that is, $q \geq 1$, the coil pitch is larger than 3 with the long end-winding as shown in Fig. 1(a). And for the condition with pole ratio of 2~5, the machines are generally equipped with fractional slot distribution winding with coil pitch of 2, as shown in Fig. 1(b). For the machine with pole ratio is smaller than 2, that is, $q \leq 1/2$, the fractional slot concentrated winding with coil pitch of 1 has been used, as drawn in Fig. 1(c). Moreover, the 18/11/7 ST-PMVM can also be treated as 18/11/11 PMSM with opening slot stator and reversal winding phase sequence [14].

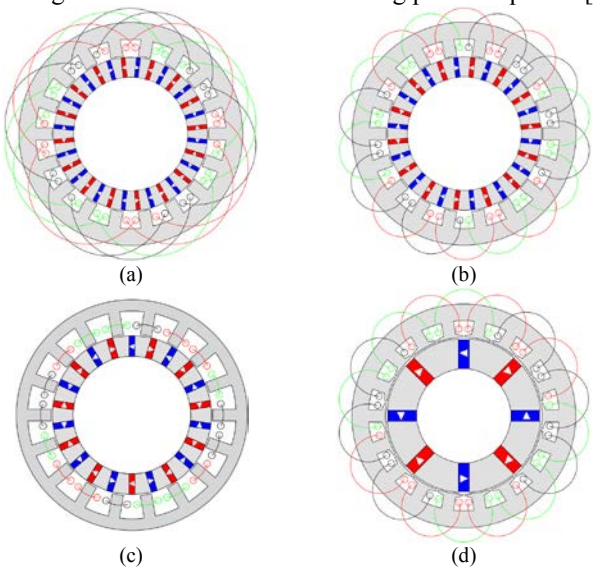

Fig. 1. Schematic of ST-PMVMs with different pole ratio. (a) *PR*=16/2. (b) *PR*=14/4. (c) *PR*=11/7. (d) The regular PMSM with 18/4/4.

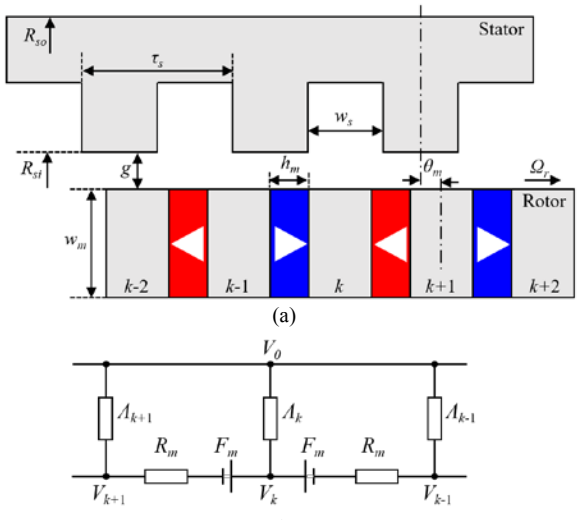

Fig. 2. Schematic and parameters of ST-PMVMs. (a) Dimensional model. (b) Equivalent magnetic circuit model.

TABLE I
MAIN PARAMETERS OF ST-PMVMS

Parameters	Value							
Stator slot number	18							
PM pole-pair	4	11	12	13	14	15	16	17
Winding pole-pair	4	7	6	5	4	3	2	1
Pole ratio	1	1.57	2	2.6	3.5	5	8	17
Coil pitch	2	1	1	2	2	3	4	9
LCM($2P_r$, Z_s)	72	198	72	234	252	90	288	306
Winding factor	0.95	0.90	0.87	0.95	0.95	1	0.95	0.96
Split ratio	0.7							
PM width/mm	16				11			
Outer diameter/mm	124							
Air-gap length/mm	0.8							
Stack length/mm	25							
PM usage/kg	0.15							
Slot areas/mm^2	1800							
Series turns	252							
Speed/(r/min)	300							
Iron material	50WW470							

B. Air-Gap Flux Density

The air-gap magnetomotive force (MMF) and permeance model has been widely used to investigate the performance of PMVMs, and the no-load air-gap flux density can be given as the product of air-gap permeance and air-gap MMF.

$$B(\theta,t)=F(\theta,t)\Lambda(\theta,t) \tag{3}$$

where B, F, Λ, θ and t represent the air-gap flux density, air-gap MMF, air-gap permeance, mechanical angle on the stator reference frame and time, respectively.

The detailed dimensional model have been labeled in Fig. 2(a), where R_{so}, R_{si}, τ_s, w_s, g, h_m and w_m are the stator outer diameter, stator inner diameter, stator slot pitch, slot opening width, air-gap length, PM thickness and PM width, respectively. And θ_m is the initial angle between stator and rotor axis, which is set as 0 in this paper. Ω_r is the mechanical rotating speed of rotor. It can be seen that the doubly salient structure has been applied in ST-PMVMs, where the air-gap permeance function can be expressed as [10]:

$$\begin{aligned}\Lambda(\theta,t)&\approx\frac{\mu_0}{g}\Lambda_s(\theta)\Lambda_r(\theta,t)\\&=\frac{\mu_0}{g}\left(\Lambda_{s0}+\Lambda_{s1}\cos(Z_s\theta)\right)\left(\Lambda_{r0}+\Lambda_{r1}\cos 2P_r(\theta-\Omega_r t)\right)\end{aligned} \tag{4}$$

where $\Lambda_s(\theta)$ and $\Lambda_r(\theta)$ are the relative permeance function when only stator and rotor are slotted. The high order harmonics with low amplitudes have been neglected, and (Λ_{s0}, Λ_{r0}) and (Λ_{s1}, Λ_{r1}) with subscripts of s and r represent the constant and fundamental permeance of stator and rotor, respectively. And the main harmonic components of air-gap permeance are listed in Table II.

TABLE II
MAJOR HARMONICS OF AIR-GAP PERMEANCE

Harmonic Order	Amplitudes	Mechanical Rotating Speed
0	$\Lambda_{s0}\Lambda_{r0}$	0
Z_s	$\Lambda_{s1}\Lambda_{r0}$	0
$2P_r$	$\Lambda_{s0}\Lambda_{r1}$	Ω_r
$Z_s\pm2P_r$	$\Lambda_{s1}\Lambda_{r1}/2$	$2P_r\Omega_r/(Z_s\pm2P_r)$

It is worth noting that the rotor iron poles have been divided into k pieces due to the interruption of adjacent PMs. As a result, the magnetic potential of each rotor iron pole should be calculated. As shown in Fig. 2(b), the equivalent magnetic circuit model has been applied to quantitatively analyze the magnetic potential V_k in each iron pole. V_0 is the stator magnetic potential, F_m and R_m represent MMF and resistance of PMs, which are given as:

$$F_m=\frac{B_r h_m}{\mu_0\mu_r},\quad R_m=\frac{h_m}{\mu_0\mu_r w_m l_{st}} \tag{5}$$

where μ_0, μ_r and l_{st} are vacuum permeability, relative permeability and stack length, respectively. And Λ_k is lumped air-gap permeance facing with the kth iron piece, which can be obtained by the integral of air-gap permeance under one rotor pole pitch $2\theta_{Pr}$.

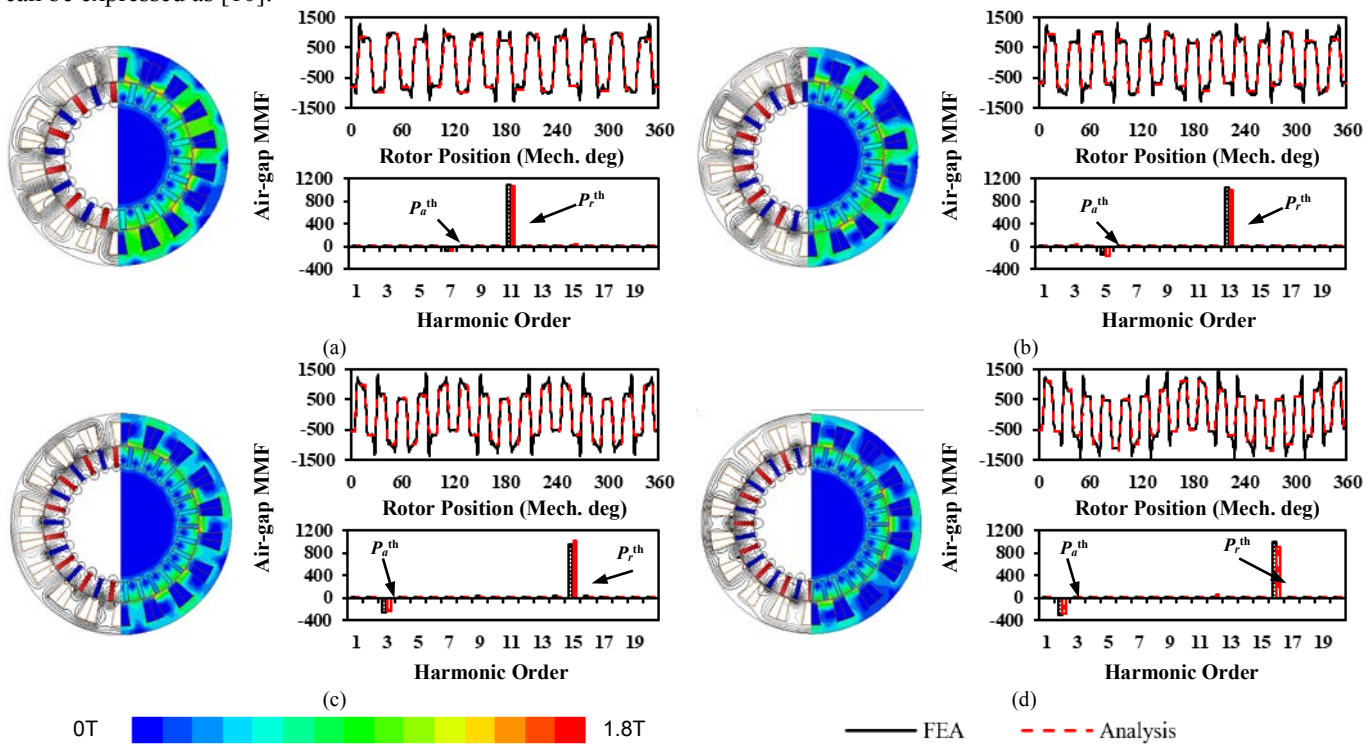

Fig. 3. Comparison of no-load air-gap flux density and air-gap MMF under different pole ratio. (a) *PR*=11/7. (b) *PR*=13/5. (c) *PR*=15/3. (d) *PR*=16/2.

$$\Lambda_k = \int_{\theta_{r,k}-\theta_{pr}}^{\theta_{r,k}+\theta_{pr}} \Lambda(\theta,t)d\theta = \Lambda_0 + \Lambda_1 \cos Z_s\left(\theta_{r,k}+\theta_m\right) \tag{6}$$

$$\Lambda_0 = 2\theta_{Pr} r_g l_{st} \Lambda_{s0} \Lambda_{r0} \frac{\mu_0}{g} \tag{7}$$

$$\Lambda_1 = 2\theta_{Pr} r_g l_{st} \Lambda_{s1} \frac{\mu_0}{g}\left(\frac{\sin\left(Z_s\theta_{Pr}\right)}{Z_s\theta_{Pr}}\Lambda_{r0} + \frac{\sin\left(Z_s\theta_{Pr}\right)}{\left(4P_r^2 - Z_s^2\right)\theta_{Pr}} Z_s \Lambda_{r1}\right) \tag{8}$$

where r_g and $\theta_{r,k}$ are the air-gap radius and relative position of kth rotor iron pole piece to the rotor axis.

$$\theta_{Pr} = \frac{\pi}{2P_r} \tag{9}$$

$$\theta_{r,k} = 2k\theta_{Pr} \tag{10}$$

Based on the equivalent magnetic circuit model, the magnetic potential of each iron pole can be expressed as:

$$\frac{V_k - F_m - V_{k+1}}{R_m} + \frac{V_k - F_m - V_{k-1}}{R_m} + V_k \Lambda_k = 0 \tag{11}$$

$$V_k = (-1)^k \frac{2F_m}{4 + R_m\Lambda_0}\left[-1 + \frac{R_m\Lambda_1 \cos Z_s\left(\theta_{r,k}+\theta_m\right)}{2 + 2\cos\dfrac{Z_s}{P_r}\pi + R_m\Lambda_k}\right] \tag{12}$$

Then, combined with the magnetic potential of rotor iron poles and PMs, the air-gap MMF along overall rotor air-gap surface can be further given as:

$$\begin{aligned} F(\theta) &= \sum_{P_i=1}^{\infty}\sum_{k=0}^{2P_r-1} \frac{2}{\pi P_i} V_k\left(1-\frac{\alpha_m}{2}\right)\cos\left(2kP_i\theta_{Pr}\right)\sin\left(P_i\theta_{Pr}\right)\cos\left(P_i\theta\right) \\ &\approx F_{Pr}\cos\left(P_r\theta\right) + F_{Pa}\cos\left(P_a\theta\right) \end{aligned} \tag{13}$$

$$\begin{aligned} F_{Pr} &= \sum_{k=0}^{2P_r-1} \frac{2}{\pi P_r} V_k\left(1-\frac{\alpha_m}{2}\right)\cos(k\pi) \\ &\approx \frac{8}{\pi}\frac{F_m}{4 + R_m\Lambda_0}\left(1-\frac{\alpha_m}{2}\right) \end{aligned} \tag{14}$$

$$F_{Pa} = \sum_{k=0}^{2P_r-1} \frac{2}{\pi P_a} V_k\left(1-\frac{\alpha_m}{2}\right)\cos\left(\frac{k\pi}{PR}\right)\sin\left(\frac{\pi}{2PR}\right) \tag{15}$$

where P_i is the harmonic order of air-gap MMF, F_{Pr} and F_{Pa} are the amplitudes of P_rth and P_ath air-gap MMF harmonics, respectively.

It can be noticed that except the harmonic F_{Pr} with the same harmonic order of rotor PMs P_rth, the harmonic F_{Pa} with order of Z_s-P_r, that is, P_ath, is also emerged. F_{Pr} is mainly determined by the PM MMF F_m, while F_{Pa} is closely associated with pole ratio. And the phase angle between which are 180°. The main harmonic components of air-gap MMF are listed in Table III.

To verify the analysis mentioned above, the air-gap MMF of ST-PMVMs with different pole ratio are analyzed and compared in Fig. 3. It can be seen that there exists the good consistency between analysis results and finite element analysis (FEA), where the air-gap MMF F_{Pa} with order of P_ath has been generated. Meanwhile, as shown in Fig. 4, with the increase of pole ratio, the amplitudes of F_{Pa} are increased, whereas the amplitudes of F_{Pr} are decreased.

Combined with (4), (14) and (15), the air-gap flux density can be expressed as (16). As shown in Fig. 5, the analysis results match well with FEA. There are two main air-gap flux density B_{Pr} and B_{Pa} with order of P_rth and P_ath, which are generated by corresponding modulation. As summarized in Table IV, the main components are in bold. It can be noticed that all the air-gap flux density produced by F_{Pa} are negative. Meanwhile, with the increase of pole ratio, the negative effects of F_{Pa} are increased, whereas the positive contribution of F_{Pr} to air-gap flux density is weakened.

$$\begin{aligned} B(\theta,t) &= \frac{g}{\mu_0}\left(\Lambda_{s0}\Lambda_{r0}F_{Pr} - \frac{\Lambda_{s1}\Lambda_{r0}}{2}F_{Pa}\right)\cos\left(P_r\theta - P_r\Omega_r t\right) \\ &\quad + \frac{g}{\mu_0}\left(\frac{\Lambda_{s1}\Lambda_{r0}}{2}F_{Pr} - \Lambda_{s0}\Lambda_{r0}F_{Pa}\right)\cos\left(P_a\theta + P_r\Omega_r t\right) \\ &= B_{Pr}\cos\left(P_r\theta - P_r\Omega_r t\right) + B_{Pa}\cos\left(P_a\theta + P_r\Omega_r t\right) \end{aligned} \tag{16}$$

$$\begin{aligned} B_{Pr}(PR) &= \frac{g}{\mu_0}\frac{2}{\pi P_r}\left(1-\frac{\alpha_m}{2}\right)\Lambda_{r0} \\ &* \sum_{k=0}^{2P_r-1} V_k\left(\Lambda_{s0}\cos(k\pi) + \frac{\Lambda_{s1}}{2}PR\cos\left(\frac{k\pi}{PR}\right)\sin\left(\frac{\pi}{2PR}\right)\right) \end{aligned} \tag{17}$$

$$\begin{aligned} B_{Pa}(PR) &= \frac{g}{\mu_0}\frac{2}{\pi P_r}\left(1-\frac{\alpha_m}{2}\right)\Lambda_{r0} \\ &* \sum_{k=0}^{2P_r-1} V_k\left(\frac{\Lambda_{s1}}{2}\cos(k\pi) + \Lambda_{s0}PR\cos\left(\frac{k\pi}{PR}\right)\sin\left(\frac{\pi}{2PR}\right)\right) \end{aligned} \tag{18}$$

Then, based on classical winding theory and electromagnetic energy conversion, back-EMF and average torque can be further expressed as:

$$E(PR) = 2\Omega_r N_c r_g l_{st} k_{total}(PR) \tag{19}$$

$$T_{ave}(PR) = 3\sqrt{2}N_c I_{rms} r_g l_{st} k_{total}(PR) \tag{20}$$

$$\begin{aligned} k_{total}(PR) &= k_{reg} + k_{ver} \\ &= k_w B_{Pr}(PR) + PRk_w B_{Pa}(PR) \end{aligned} \tag{21}$$

where N_c, I_{rms}, k_w, k_{reg}, k_{ver} and k_{total} are the coil turns per phase, phase current RMS value, winding coefficient, regular torque coefficient, modulation torque coefficient and total torque coefficient, respectively.

From (19) and (20), it can be seen that both back-EMF and average torque are determined by total torque coefficient k_{total}, which is the function of pole ratio PR. And k_{total} is the superposition of regular torque coefficient and modulation torque coefficient. Both the harmonics of B_{Pr} and B_{Pa} contribute the production of average torque, which are named as the working harmonics in this paper. Pole ratio as the amplification factor has been emerged in modulation torque, which reflects magnetic field modulation effects. Based on the analysis mentioned above, with the increase of pole ratio, the amplitudes of B_{Pr} and B_{Pa} are decreased duo the increase of F_{Pa} and the decrease of F_{Pr}. That is, there is the optimal pole ratio to achieve the maximum electromagnetic torque.

TABLE III
MAIN HARMONICS OF AIR-GAP MMF

Harmonic Order	Amplitudes	Mechanical Rotating Speed
P_r	F_{Pr}	Ω_r
P_a	F_{Pa}	$-\Omega_r P_r/P_a$

TABLE IV
MAIN HARMONICS OF AIR-GAP FLUX DENSITY

Harmonic order	Amplitudes	Mechanical rotating speed	Sources
P_r	$\boldsymbol{\Lambda_{s0}\Lambda_{r0}F_{Pr}}$	Ω_r	F_{Pr}
	$\boldsymbol{-\Lambda_{s1}\Lambda_{r0}F_{Pa}/2}$		F_{Pa}
	$\Lambda_{s0}\Lambda_{r1}F_{Pr}/2$		F_{Pr}
P_a	$\boldsymbol{-\Lambda_{s0}\Lambda_{r0}F_{Pa}}$	$-\Omega_r P_r/P_a$	F_{Pa}
	$\boldsymbol{\Lambda_{s1}\Lambda_{r0}F_{Pr}/2}$		F_{Pr}
	$\Lambda_{s1}\Lambda_{r1}F_{Pr}/4$		F_{Pr}

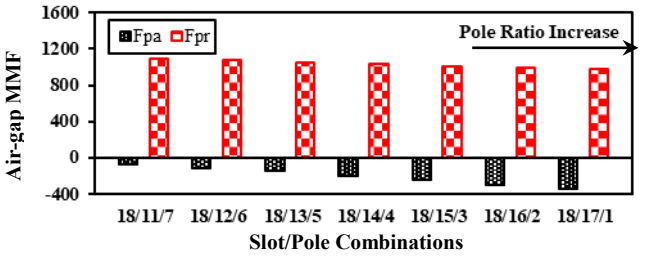

Fig. 4. Comparison of air-gap MMF under different pole ratio.

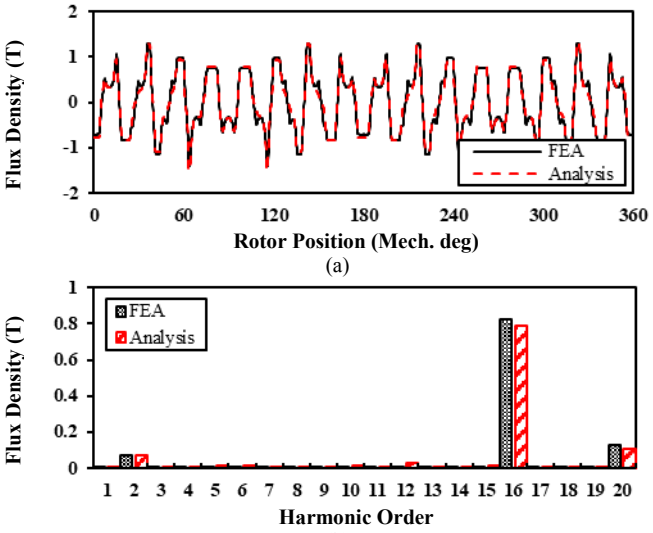

Fig. 5. Air-gap flux density of ST-PMVMs with pole ratio of 16/2.

III. DIMENSION PARAMETER SELECTION

Based on the analysis mentioned above, it is indicated that the air-gap MMF of ST-PMVMs has introduced multiple harmonics due to doubly salient air-gap structure. Therefore, it is necessary to comprehensively analyze the influence of critical air-gap dimension parameters, including stator slot opening ratio, PM pole-arc ratio and split ratio on air-gap MMF, air-gap flux density and machine performance.

By properly choosing the air-gap dimension parameters, the electromagnetic performance of ST-PMVMs can be further improved. Moreover, the coupling between dimension parameter and pole ratio is revealed, which is useful to provide the design guidance of ST-PMVM under different pole ratio. And total torque coefficient k_{total} are selected as the indicator to estimate machine performance.

A. Stator Slot Opening Ratio

For the design of ST-PMVMs, the stator slot opening ratio should be carefully selected, which is related to the air-gap MMF of F_{Pr} and F_{pa} at the same time. At first, the influence of stator slot opening ratio on air-gap MMF and k_{total} are investigated, where other parameters are kept the same for a fair comparison.

According to (14) and (15), F_{Pr} is inversely linked to Λ_{s0}, while F_{Pa} is related to the ratio of $\Lambda_{s1}/\Lambda_{s0}$. As depicted in Fig. 6(a), the stator relative constant permeance Λ_{s0} has an opposite relationship with slot opening ratio, and relative fundamental permeance Λ_{s1} increase to their peak value and then drop. Moreover, as shown in Fig. 6(b), with the increase of slot number, Λ_{s1} is much smaller than Λ_{s0}, that is, the modulation effects have be weakened. As a result, it can be seen in Fig. 7(a) that F_{Pr} is increased with the increase of stator slot opening due to the decrease of Λ_{s0}. And F_{Pa} is increased firstly and decreased, where the variation trend is consistent to $\Lambda_{s1}/\Lambda_{s0}$.

Moreover, the ratios of F_{Pa}/F_{Pr} under different stator slot opening ratio are compared in Fig. 7(b), where the negative effects of F_{Pa} is much serious at the slot opening ratio around 0.7. Meanwhile, it can be noticed that the proportion of F_{Pa} is significant at high pole ratio, that is, the negative contribution of which is serious. For the same pole ratio, the ratios of F_{Pa}/F_{Pr} is decreased with the increase of stator slot number.

Further, the coefficients k_{total} under different slot opening ratio and pole ratio are calculated. It can be noticed in Fig. 8(a) that there is the optimal slot opening around 0.3 which can balance working flux density and pole ratio so as to achieve the maximum back-EMF. For the same pole ratio, the smaller stator slot number is recommendable. Moreover, it can be seen in Fig. 8(b) that with the increase of slot opening and pole ratio, the contribution of regular torque components is decreased. Especially, at the slot opening ratio 0.8, the ratios are minimum, that is, the proportions of modulation torque components are maximum. And the ratios of k_{reg}/k_{total} are increased with the increase of slot number due to $\Lambda_{s1}/\Lambda_{s0}$ is decreased as shown in Fig. 6(b).

Therefore, for the design of ST-PMVMs, the preferable stator slot opening ratio is around 0.3. And for the same pole ratio, the smaller stator slot number is preferable.

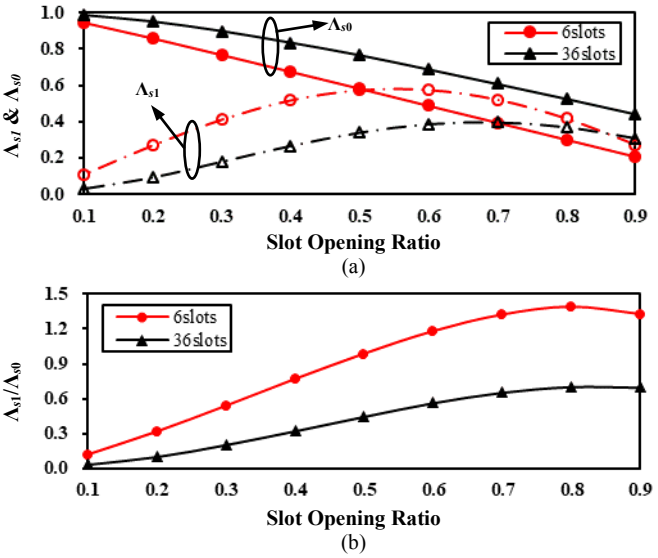

Fig. 6. Comparison of stator relative permeance with different slot opening ratio. (a) Λ_{s1} & Λ_{s0}. (b) $\Lambda_{s1}/\Lambda_{s0}$.

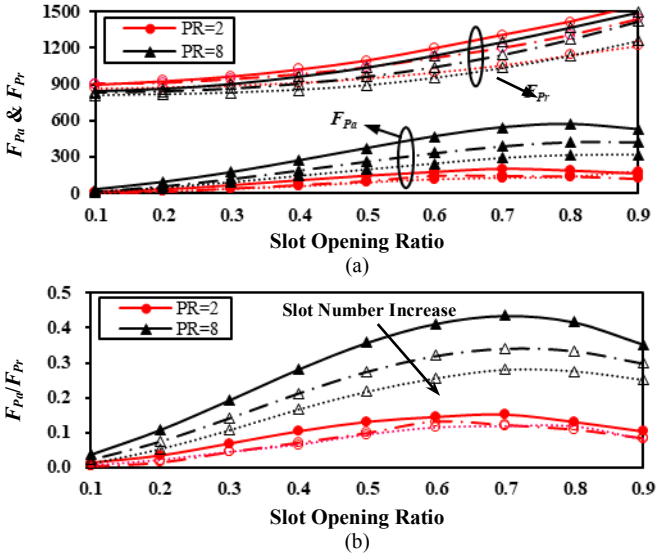

Fig. 7. Comparison of rotor magnetic potential with different slot opening ratio. (a) F_{Pa} & F_{Pr}. (b) F_{Pa}/F_{Pr}.

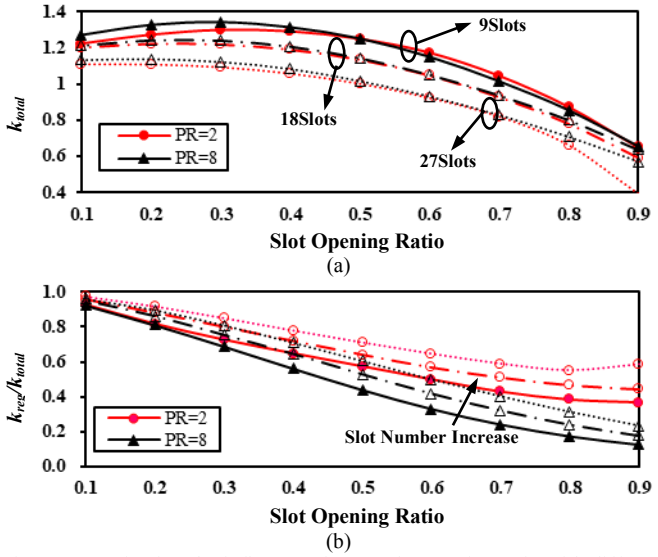

Fig. 8. Investigation the influence of stator slot opening ratio with different pole ratio. (a) k_{total}. (b) k_{reg}/k_{total}.

B. PM Pole-Arc Ratio

The influence of PM pole-arc on machine performance are analyzed and compared. The air-gap MMF variation against PM pole-arc is shown in Fig. 9, where F_{Pr}, F_{Pa} and the ratio of F_{Pa}/F_{Pr} are increased with the increase of PM pole-arc ratio due to the decrease of Λ_{r0}. Further, the curves of k_{total} versus PM pole-arc ratio are drawn in Fig. 10(a). It can be found that PM pole-arc is mainly determined by the stator slot number. That is, for the fixed PM volumes and stator slot number, the optimal PM arc-pole is identical under different pole ratio. And the optimal PM pole-arc is increased with the increase of stator slot number, where the recommendable PM pole-arc in 9 slots, 18slots and 27slots stator structure are 0.133, 0.266 and 0.399, respectively.

Moreover, the ratio of k_{reg}/k_{total} are shown in Fig. 10(b). For the same pole ratio, the k_{reg}/k_{total} is increased with the increase with stator slot number due to the decrease of fundamental permeance Λ_{s1}. For the same stator slot number, the proportion of k_{reg} is decreased in the high pole ratio models.

C. Split Ratio

The influence of split ratio on machine performance are investigated. To have a deep insight, the models compared in Fig. 11 covering different pole ratio and different slot/pole combination. For a fair comparison, the current density of all the models are kept identical. It can be seen in Fig. 11 that with the increase of armature winding pole pair, the optimal stator yoke is decreased and the optimal split ratio is increased. Take the model 9/6/3 with pole ratio of 2 and model 27/24/3 with pole ratio of 8 as examples. Although the pole ratio of which is obviously different, they also have the similar optimal split ratio due to the same armature winding pole pair of 3. In other words, the coupling between pole ratio and split ratio is weak.

Split ratio is mainly determined by the pole-pair of armature winding, whereas the influence of pole ratio and stator slot number on split ratio can be neglected.

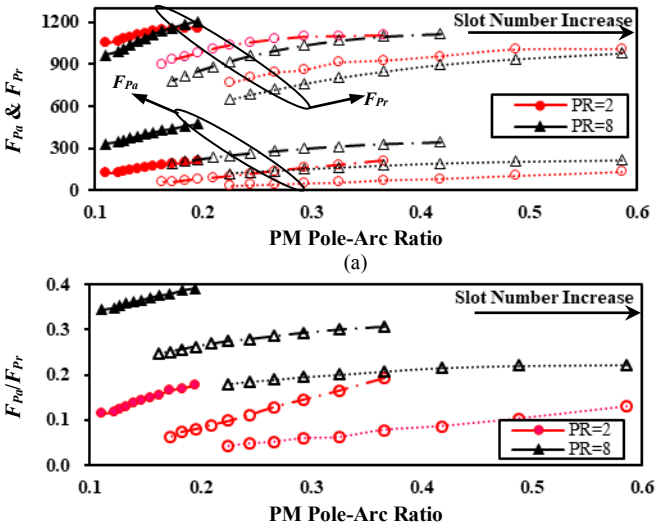

Fig. 9. Investigation the influence of PM pole-arc ratio on the air-gap magnetic potential. (a) F_{Pa} & F_{Pr}. (b) F_{Pa}/F_{Pr}.

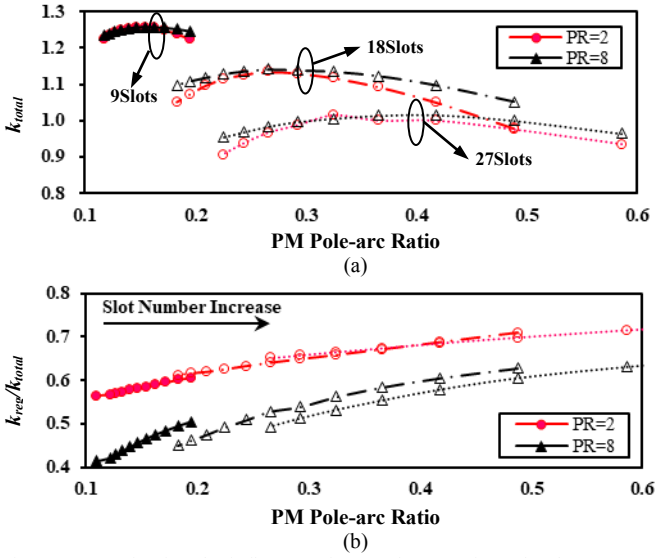

Fig. 10. Investigation the influence of PM pole-arc ratio under the same PM volumes. (a) k_{total}. (b) k_{reg}/k_{total}.

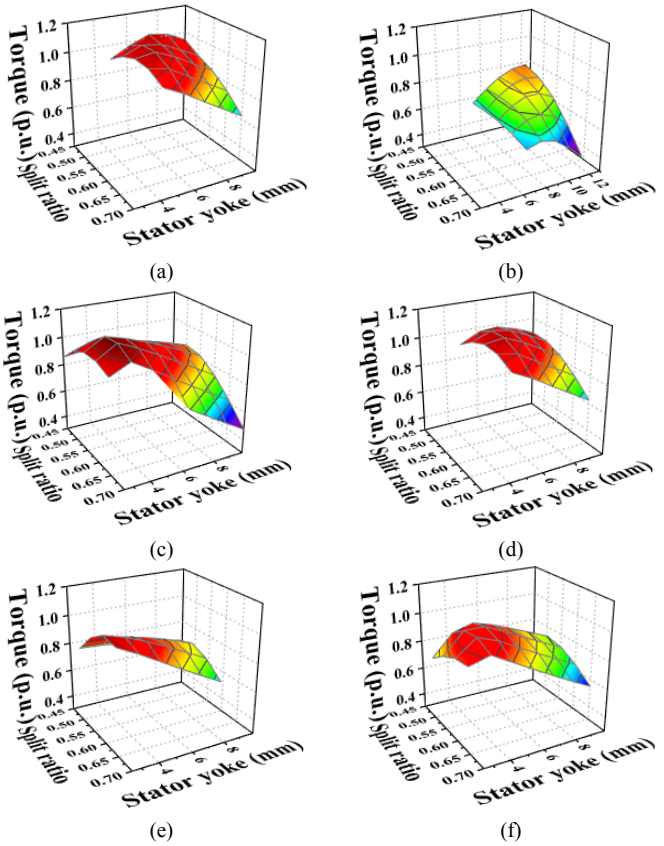

Fig. 11. Comparison of torque capability under the same current density. (a) 9/6/3. (b) 9/8/1. (c) 18/12/6. (d) 18/16/2. (e) 27/18/9. (f) 27/24/3.

IV. Performance Analysis

In this section, ST-PMVMs with different pole ratio and winding structure are comprehensively compared to determine the optimal pole ratio. For direct-drive application, the estimation indicators cover average torque, cogging torque, overload capability and power factor. In other words, the optimal pole ratio is derived from multi-objective function as follows:

$$PR_{optimal} = f\left(k_1 Max\left(T_{ave}\left(PR\right)\right) + k_2 Min\left(T_{ripples}\left(PR\right)\right) + k_3 Max\left(PF\left(PR\right)\right)\right) \quad (22)$$

where $Max\ (T_{ave})$, $Min\ (T_{ripples})$, $Max\ (PF)$ represent maximum average torque, minimum cogging torque and maximum power factor. And k_1, k_2 and k_3 are the weight coefficient to estimate machine performance, which is depend on the detailed machine working conditions.

For a fair comparison, all the models have the same stator outer diameter, stack length and PM usage. Moreover, stator slot opening and PM pole-arc ratio, have been optimized to achieve the maximum electromagnetic torque. The main difference between them is the pole ratio and winding connection, where the coil pitch, that is, the end-winding length, is increased with the increase of pole ratio. And the main parameters are listed in Table I. And the regular PMSM has also been compared as a counterpart.

A. No-Load Performance

The detailed working flux density, including B_{Pa} and B_{Pr}, derived from F_{Pa} and F_{Pr} are shown in Fig. 12(a) and (b), respectively. It can be observed that with the increase of pole ratio, both the amplitudes of B_{Pa} and B_{Pr} are decreased, due to the negative contribution of air-gap MMF F_{Pa} is increased and the positive contribution of F_{Pr} is decreased.

From (20) and (21), it can be seen that both back-EMF and average torque are determined by k_{total}, which is the function of pole ratio PR. Thus, k_{total} has been selected as the estimate indicator to determine $Max\ (T_{ave})$.

$$Max\left(T_{ave}\left(PR\right)\right) = f\left(k_{total}\left(PR\right)\right) \quad (23)$$

It can be seen in Fig. 12 that the air-gap flux density analysis results match well with FEA, where the model with pole ratio of 5 can achieve the maximum EMF and torque. Moreover, the models with pole ratio of 2.6 and 3.5 can also obtain the comparable amplitudes.

However, the model with high pole ratio of 8 and 17 have lower total working flux density amplitudes, due to pole ratio amplification factor cannot offset the serious decrease of B_{Pa} and B_{Pr}. And the model with pole ratio of 2 has the minimum amplitudes, which is due to the winding factor of which is the minimum.

The EMF waveforms are compared in Fig. 13, and it can be noticed that the variation of EMF are consistent to k_{total}, where the model with pole ratio of 5 has the maximum EMF fundamental amplitudes. Compared to regular PMSM, the fundamental amplitudes have been increased 44.39%.

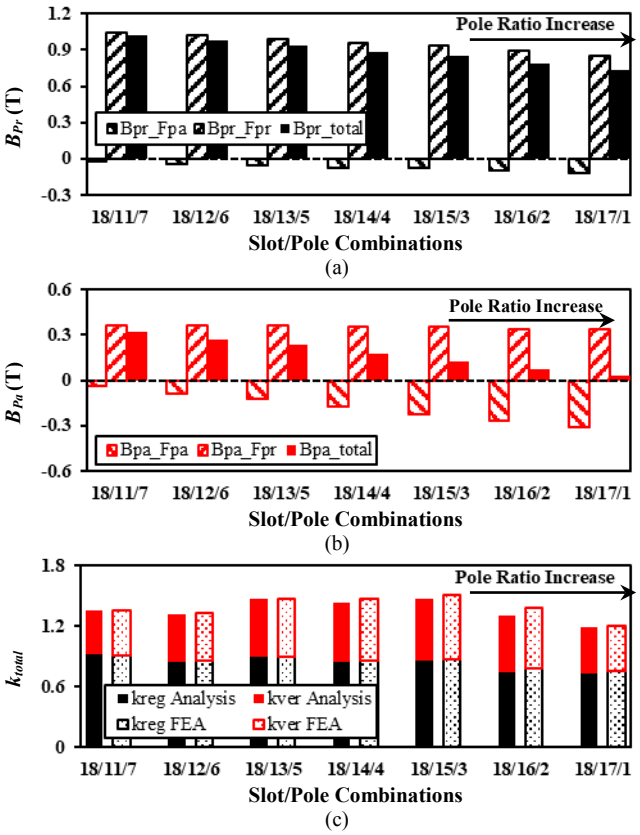

Fig. 12. Comparison of torque coefficient. (a) B_{Pa}. (b) B_{Pr}. (c) k_{total}.

And the cogging torque waveforms have been shown in Fig. 14, it is worth noting that the models with pole ratio of 2 and 5

have obvious cogging torque. Cogging torque can be estimated by the lowest common multiple LCM of stator slot number and PM pole-pair number, that is, LCM ($2P_r$, Z_s). Further, it can be expressed as:

$$Min\left(T_{ripples}\left(PR\right)\right) = f\left(LCM\left(2PR, PR+1\right)\right) \tag{24}$$

As depicted in Table I, the models with pole ratio of 2 and 5 have small LCM ($2P_r$, Z_s) and high cogging torque. Other models have the preferable cogging torque.

B. On-Load Performance

And the on-load performance of ST-PMVMs with different pole ratio are analyzed and compared. As shown in Fig. 15, the torque waveforms at current density of 6 A/mm^2 are compared, where the model with pole ratio of 2.6 and 3.5 can acquire the high average torque and low torque ripples at the same time.

Further, taking coil pitches into consideration, the torque against stack length of various ST-PMVMs under the same copper losses have been analyzed. It can be noticed in Fig. 16 that when stack length is small, the models with pole ratio range of 1~2 are competitive due to coil pitch is 1. With the increase of stack length, the superiority of models with pole ratio range of 2~5 is gradually reflected where the coil pitch is 2.

In Fig. 17, the overload capability of various models are compared. It can be noticed that with the increase of pole ratio, the models are easier to get saturation, which is due to the larger inductance and armature reaction. Among which, the model with pole ratio of 2.6 can get the optimal overload capability, which is preferable for the direct-drive application.

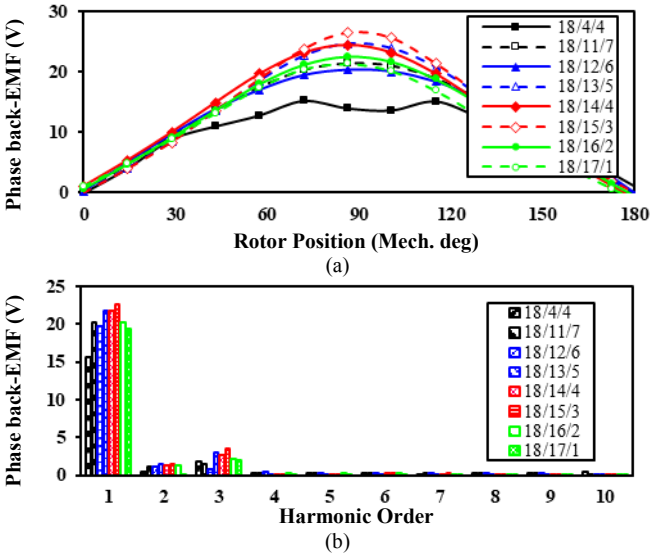

Fig. 13. Comparison of back-EMF. (a) Waveforms. (b) FFT.

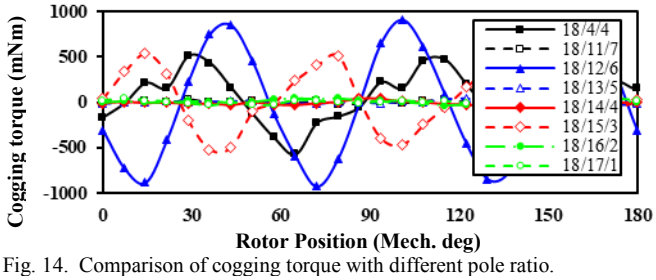

Fig. 14. Comparison of cogging torque with different pole ratio.

Moreover, the power factor of various models are compared in Fig. 18. It can be observed that with the increase of pole ratio, the power factor is sharply decreased. Among which, regular PMSM has the maximum power factor. However, the high pole ratio ST-PMVMs suffer from serious low power factor.

It has been revealed in [16]-[17] that there exists the inverse relationship between power factor and pole ratio, which can be given as:

$$Max\left(PF\left(PR\right)\right) = f\left(\frac{1}{PR} + \frac{\Lambda_1}{2\Lambda_0}\right) \tag{25}$$

Combined with (22) to (25), model 18/13/5 with pole ratio of 2.6 can balance the torque capability, torque ripple and power factor. Thus, it is selected as the optimal candidate at the fixed motor size.

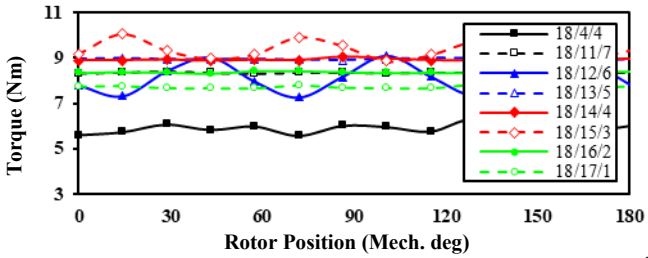

Fig. 15. Comparison of torque waveforms under current density of 6 A/mm^2.

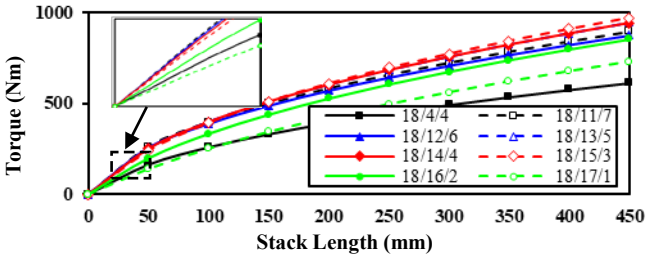

Fig. 16. Comparison of average torque with different stack length.

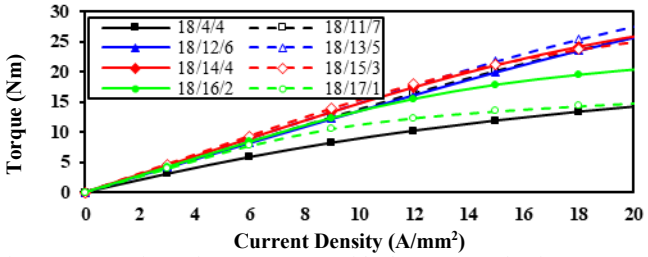

Fig. 17. Comparison of average torque with phase current density.

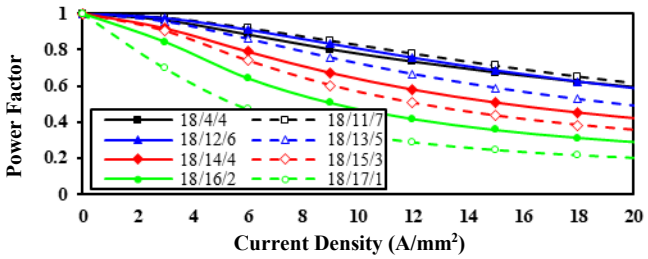

Fig. 18. Comparison of power factor with phase current density.

TABLE V
KEY PARAMETERS OF ST-PMVMS UNDER DIFFERENT POWER RATING

Parameters	Scaling I	Scaling II	Scaling III
Outer radius/mm	100	1000	3000
Air-gap length/mm	1	2	3
Stack length/mm	25	50	100
PM consumption/kg	0.12	21	386

V. Machine Scaling Effect

In section IV, the optimal pole ratio is determined under the fixed outer diameter of 124 mm. In this section, the influence of machine size on optimal pole ratio is further investigated, where three different power rating has been selected. And the detailed dimension parameters are listed in Table V.

With the increase of power rating, air-gap length is increased, which is one of the most sensitive dimension parameter. As a result, the variation of air-gap permeance under different air-gap length is analyzed first.

It can be noticed in Fig. 19 that with the increase of air-gap length, air-gap fundamental permeance is significantly lower than air-gap constant permeance. In other words, the modulation effect has been weakened in large machine scaling. Further, the variation of air-gap MMF under different machine scaling has been presented in Fig. 20. With the increase of pole ratio, the negative influence of F_{pa} is increased. For the large power rating having long equivalent air-gap, the negative influence of which is much serious. It can be noticed in Fig. 21 that the variation of total torque coefficient k_{total} under different power rating is similar, where the maximum value can be produced by the model 18/15/3 with pole ratio of 5. Moreover, the model 18/13/5 and 18/14/4 can also have the high amplitudes of k_{total}, which means the average torque of which is preferable.

Further, taking torque ripples, end-winding length, power factor and overload capability into consideration, the model 18/13/5 with pole ratio 2.6 can also be the better candidate for different power rating.

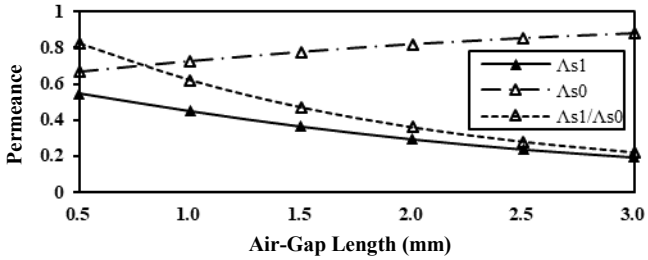

Fig. 19. Comparison of permeance under different air-gap length.

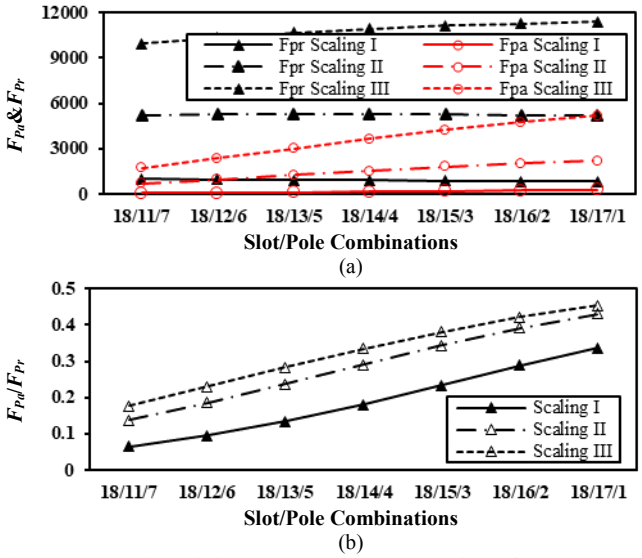

Fig. 20. Comparison of air-gap MMF. (a) F_{Pa} & F_{Pr}. (b) F_{Pa}/F_{Pr}.

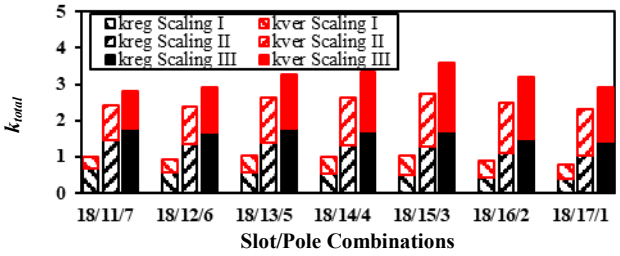

Fig. 21. Comparison of torque coefficient under different motor size.

VI. Experimental Validation

To verify the analysis mentioned above, an 18/13/5 ST-PMVM prototype with pole ratio of 2.6 is manufactured and tested. The stator, rotor and shaft of ST-PMVM are shown in Fig. 22, and Fig. 23 shows the platform for experiment. The back-EMF at the base speed of 300 rpm are measured and compared with FEA results, where the good agreement can be achieved, as depicted in Fig. 24. Moreover, the variation of torque/power factor against current density are drawn in Fig. 25. It can be seen that the torque linearity of prototype with pole ratio of 2.6 is good. Meanwhile, the power factor of which can maintain above 0.95.

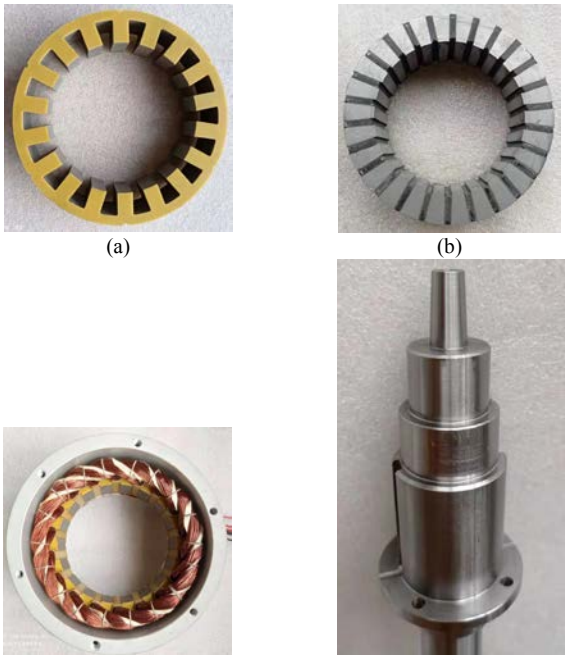

(a) (b) (c) (d)

Fig. 22. Photo of 18/13/5 ST-PMVM prototype. (a) Stator. (b) Rotor. (c) Wound stator. (d) Shaft.

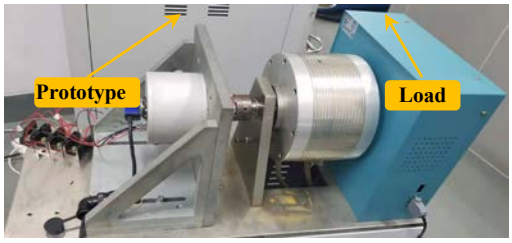

Fig. 23. Set-up for experimentation.

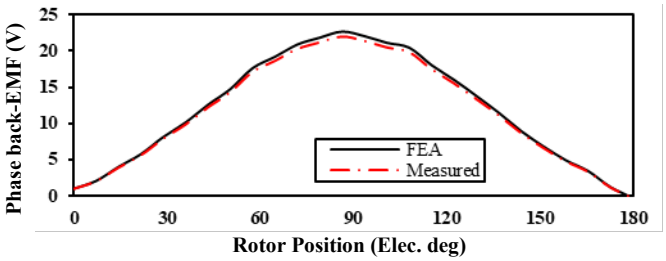

Fig. 24. Comparison of phase back-EMF at base speed of 300rpm.

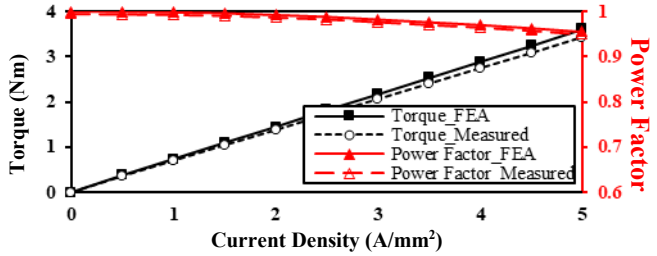

Fig. 25. Comparison of average torque and power factor.

VII. Conclusion

In this paper, a comprehensive comparison of ST-PMVMs under different pole ratio is carried out. According to the equivalent magnetic circuit model, the air-gap MMFs, air-gap flux density and torque capability of ST-PMVMs are deeply investigated, and the optimal pole ratio is determined. Some conclusions can be given as follows.

1) Due to the doubly salient structure, the air-gap MMF introduces an extra harmonic component F_{Pa} with the pole-pair of stator winding P_a, which would produce negative torque.

2) With the increase of pole ratio, the negative contribution of F_{Pa} is increased, which would deteriorate the advantage of flux modulation effects brought by the torque amplification coefficient pole ratio. Thus, the key to determine the optimal pole ratio of ST-PMVM is to balance the extra air-gap MMF harmonic F_{Pa} and pole ratio.

3) The influence of critical dimension parameters on machine performance has been investigated. To balance air-gap MMF harmonic F_{Pa} and pole ratio, the preferable stator slot opening ratio of ST-PMVM is around 0.3, which is smaller than surface-mounted PMVM.

4) Taking cogging torque, average torque, torque density, overload capability and power factor into consideration, the ST-PMVM having 18 stator slots with pole ratio 2.6 can be the better candidate for the direct-drive application.

References

[1] K. T. Chau, C. C. Chan and C. Liu, "Overview of Permanent-Magnet Brushless Drives for Electric and Hybrid Electric Vehicles," in IEEE Transactions on Industrial Electronics, vol. 55, no. 6, pp. 2246-2257, June 2008.

[2] Z. Q. Zhu and D. Howe, "Electrical Machines and Drives for Electric, Hybrid, and Fuel Cell Vehicles," in Proceedings of the IEEE, vol. 95, no. 4, pp. 746-765, April 20072.

[3] X. D. Xue, K. W. E. Cheng, T. W. Ng and N. C. Cheung, "Multi-Objective Optimization Design of In-Wheel Switched Reluctance Motors in Electric Vehicles," in IEEE Transactions on Industrial Electronics, vol. 57, no. 9, pp. 2980-2987, Sept. 2010.

[4] J. Nerg, M. Rilla, V. Ruuskanen, J. Pyrhönen and S. Ruotsalainen, "Direct-Driven Interior Magnet Permanent-Magnet Synchronous Motors for a Full Electric Sports Car," in IEEE Transactions on Industrial Electronics, vol. 61, no. 8, pp. 4286-4294, Aug. 2014.

[5] G. Pellegrino, A. Vagati, P. Guglielmi and B. Boazzo, "Performance Comparison Between Surface-Mounted and Interior PM Motor Drives for Electric Vehicle Application," in IEEE Transactions on Industrial Electronics, vol. 59, no. 2, pp. 803-811, Feb. 2012.

[6] D. G. Dorrell, A. M. Knight, L. Evans and M. Popescu, "Analysis and Design Techniques Applied to Hybrid Vehicle Drive Machines—Assessment of Alternative IPM and Induction Motor Topologies," in IEEE Transactions on Industrial Electronics, vol. 59, no. 10, pp. 3690-3699, Oct. 2012.

[7] P. Han, M. Cheng, Y. Jiang and Z. Chen, "Torque/Power Density Optimization of a Dual-Stator Brushless Doubly-Fed Induction Generator for Wind Power Application," in IEEE Transactions on Industrial Electronics, vol. 64, no. 12, pp. 9864-9875, Dec. 2017.

[8] K. Xie, D. Li, R. Qu, X. Ren, M. R. Shah and Y. Pan, "A New Perspective on the PM Vernier Machine Mechanism," in IEEE Transactions on Industry Applications, vol. 55, no. 2, pp. 1420-1429, March-April 2019.

[9] B. Kim and T. A. Lipo, "Operation and Design Principles of a PM Vernier Motor," in IEEE Transactions on Industry Applications, vol. 50, no. 6, pp. 3656-3663, Nov.-Dec. 2014.

[10] T. Zou, D. Li, R. Qu and D. Jiang, "Performance Comparison of Surface and Spoke-Type Flux-Modulation Machines With Different Pole Ratios," in IEEE Transactions on Magnetics, vol. 53, no. 6, pp. 1-5, June 2017.

[11] B. Kim and T. A. Lipo, "Analysis of a PM Vernier Motor With Spoke Structure," in IEEE Transactions on Industry Applications, vol. 52, no. 1, pp. 217-225, Jan.-Feb. 2016.

[12] X. Ren, D. Li, R. Qu, Z. Yu and Y. Gao, "Investigation of Spoke Array Permanent Magnet Vernier Machine With Alternate Flux Bridges," in IEEE Transactions on Energy Conversion, vol. 33, no. 4, pp. 2112-2121, Dec. 2018.

[13] R. Cao, M. Cheng, C. Mi, W. Hua, X. Wang and W. Zhao, "Modeling of a Complementary and Modular Linear Flux-Switching Permanent Magnet Motor for Urban Rail Transit Applications," in IEEE Transactions on Energy Conversion, vol. 27, no. 2, pp. 489-497, June 2012.

[14] Z. Q. Zhu and Y. Liu, "Analysis of Air-Gap Field Modulation and Magnetic Gearing Effect in Fractional-Slot Concentrated-Winding Permanent-Magnet Synchronous Machines," in IEEE Transactions on Industrial Electronics, vol. 65, no. 5, pp. 3688-3698, May 2018.

[15] D. Li, T. Zou, R. Qu and D. Jiang, "Analysis of Fractional-Slot Concentrated Winding PM Vernier Machines With Regular Open-Slot Stators," in IEEE Transactions on Industry Applications, vol. 54, no. 2, pp. 1320-1330, March-April 2018.

[16] Y. Zhao, D. Li, X. Ren and R. Qu, "Investigation of Permanent Magnet Vernier Machines from Armature Field Perspective," in IEEE Journal of Emerging and Selected Topics in Power Electronics, Early Access.

[17] D. K. K. Padinharu, G. -J. Li, Z. -Q. Zhu, R. Clark, A. S. Thomas and Z. Azar, "System-Level Investigation of Multi-MW Direct-Drive Wind Power PM Vernier Generators," in IEEE Access, vol. 8, pp. 191433-191446, 2020.

Yu Zhao (Student Member, IEEE) was born in China. She received the B.E.E. degree in electrical engineering from Southwest Jiaotong University, Chengdu, China, in 2017. She is currently working toward the Ph.D. degree in electrical engineering at Huazhong University of Science and Technology, Wuhan, China.

Her research interests include design and analysis of flux-modulation permanent-magnet machines.

Dawei Li (Senior Member, IEEE) was born in China. He received the B.E.E. degrees in electrical engineering from Harbin Institute of Technology, Harbin, China, in 2010 and the Ph.D. degree in electrical engineering from Huazhong University of Science & Technology, in 2015. In Jul. 2015, he joined Huazhong University of Science &Technology, Wuhan, China.

Dr. Li has authored over 60 published technical papers and is the holder of over 10 patents/patent applications. He was recipient of the Best Poster Presentation Award from the XXII th International Conference on Electrical Machines (ICEM 2016), and Hubei Province Excellent Doctoral Dissertation (2016), China. His research areas include the design and analysis of flux-modulation permanent-magnet machines.

Xiang Ren was born in Hunan, China. He received the B.Eng. and Ph.D. degrees in electrical engineering from the Huazhong University of Science and Technology, Wuhan, China, in 2014 and 2019, respectively.

He is currently a Postdoc with the Huazhong University of Science and Technology. His research interests include design and analysis of flux modulation machines.

Ronghai Qu (Fellow, IEEE), Fellow of China Electrotechnical Society, received his B.E. and M.S. degrees from Tsinghua University, Beijing, China, in 1993 and 1996, respectively, and the Ph.D. degree in electrical engineering from University of Wisconsin-Madison in 2002. He had been with the General Electric (GE) Global Research Center, Niskayuna, NY as a Senior Electrical Engineer with the Electrical Machines and Drives Laboratory from 2003 to 2010. He was the recipient of 11 GE GRC awards including EPST Technical Achievement Award, Outstanding Teamwork and Management Award. In 2010 he joined Huazhong University of Science & Technology, Wuhan, China. He is currently director of State and Province Joint Engineering Research Center of Novel Electrical Machines, and director of Center for Advanced Electrical Machines and Drives (CAEMD). From 2012 to 2016, he served as deputy dean of school of Electrical & Electronic Engineering. He is currently a member of ICEM NPO AdCom and the chair of IEEE Industry Application Society (IAS) Wuhan Chapter. His research interests include Design and Drive of Electrical Machines. He has published over 400 technical papers including 14 IEEE award papers and holds over 170 patents. Dr. Qu is also a winner of several other awards including 2020 Science and Technology Invention Award (1st prize) from China Electrotechnical Society, the 7th Nagamori Awards from Nagamori Foundation, Japan, 2021, and 2 gold Medals from the 47th Exhibition of Inventions of Geneva, 2019, the 12th Innovation and Entrepreneurial Figure Award, China Association of Inventions, 2022.

Jianbo Sun received the B.S. and Ph.D. degrees from the Huazhong University of Science and Technology, Wuhan, China, in 1998 and 2005, respectively, where he is currently an Associate Professor with the School of Electrical and Electronic Engineering.

His research interests include new type electric machine's design and control.

Ping Yu is the founder, chairman, CEO and chief engineer of Jing-Jin Electric Technology Co., Ltd.. With bachelor's degree in automotive engineering of Tsinghua University, master's degree in automotive engineering of University of Michigan, and master's degree in Business Administration of Massachusetts Institute of Technology, he is one of the Recruitment Program of Global Expert and a Professorate Senior Engineer. He worked for General Motors in the United States and served successively as senior engineer and manager of global hybrid power strategy and planning. Returned from the United States in 2007, Yu Ping has founded Jing-Jin Electric Technology Co., Ltd.. In a few short years, he leads the young company to realize the large-scale industrialization of driving motors and powertrains of new energy vehicles in China and exports supporting products for international high-end models, which has built a well-known international brand. He has more than 30 patents in China, the United States, Japan and Europe.